

# Winding coupling phase for pseudo-spin-derived topological photonics

Received: 15 December 2024

Tianyuan Liu <sup>1,2</sup>, Min Qiu <sup>2,3,4</sup>  & Wei Yan <sup>2,3</sup> 

Accepted: 4 December 2025

Published online: 24 December 2025

 Check for updates

Topological phases derived from spin or pseudo-spin typically leverage specific effects like spin-orbit interaction or antiferromagnetism. Here, we propose a flexible theoretical framework capable of designing pseudo-spin-derived topological phases. We reveal that the evanescent coupling between nearby resonators exhibits a  $\pi_1(S^1)$  topology characterized by a quantized coupling winding number. By tailoring the coupling winding number in photonic crystals, we propose silicon-on-insulator designs for the spin-valley Hall phase (SVHP), its anomalous variant, the anomalous Hall phase, and anti-helical edge states. Notably, the SVHP is obtained in a non-antiferromagnetic system without the need of time-reversal symmetry breaking, and the anti-helical edge states are designed independently of next-nearest coupling tuning. The results are compatible with conventional fabrication processes, demonstrating the simplicity and versatility of this framework and its potential for applications in spin-valley protected light transport and slow light guiding.

Topology, a mathematical subject that focuses on invariant properties of spaces under continuous deformations, has proven to be a fruitful perspective for deriving novel physical phenomena<sup>1–6</sup>. One notable example is topologically protected edge states emerged at interfaces between two materials with distinct topological invariants<sup>7–10</sup>. Standing on the advanced nanofabrication technologies<sup>11–14</sup> and the accumulated capabilities of photonic crystals<sup>15,16</sup>, photonics has emerged as a vibrant, configurable platform to study topological physics<sup>1,2</sup>. Moreover, the topological advantages of the edge states have also found applications in light transport<sup>8,17–19</sup> and lasing<sup>20–22</sup>.

Among various approaches to realize topological phases in photonics, the pseudo-spin degree of freedom (DOF) has been widely used<sup>17,23–28</sup>. The photonic pseudo-spin is typically constructed by a pair of orthogonal modes, e.g., clockwise and anti-clockwise circulated angular-momentum modes<sup>17,29</sup>, and bonding and anti-bonding modes<sup>30,31</sup>. These modes correlate to each other like intrinsic spins of photons (i.e., left- and right-handed circular polarization states), while showing better resistance to spin mixing than the intrinsic spins. Based on this, various photonic pseudo-spin-derived topological phases, such as spin Hall<sup>32,33</sup> and spin-valley Hall phases<sup>27,28</sup>, have been proposed, where the spin-

dependent mass terms are induced by optical spin-orbit interaction<sup>32,34</sup> and nonlinearity<sup>27</sup>, respectively. In addition, Hall<sup>17</sup> and the anomalous Hall phases<sup>25</sup> in spin subspaces have been realized by introducing effective gauge fields through auxiliary coupling components such as racetrack micro-ring resonators (MRRs). Nevertheless, these strategies are mostly tailored to specific phases. Developing a general framework that encompasses a variety of pseudo-spin-derived topological phases would provide broad utility for simple photonic realizations.

In this study, a framework, capable of realizing various pseudo-spin-derived topological phases, is reported based on a central concept—the coupling winding number  $W$ .  $W$  is a topological invariant, which characterizes the net number of times that a complex-valued coupling coefficient winds around the origin as one resonator evolves a closed path around another resonator in real space. For angular momentum (AM) modes,  $W$  depends solely on the AM quantum numbers, and reverses its sign as the AM numbers flip (that is, pseudo-spin flips). Manipulating  $W$  of the AM modes allows for a flexible control of coupling phases between resonators in photonic crystals. This approach enables us to realize a broad range of pseudo-spin-derived topological phases, including the spin-valley Hall phase

<sup>1</sup>College of Information Science and Electronic Engineering, Zhejiang University, Hangzhou, Zhejiang, China. <sup>2</sup>Zhejiang Key Laboratory of 3D Micro/Nano Fabrication and Characterization, Department of Electronic and Information Engineering, School of Engineering, Westlake University, Hangzhou, Zhejiang, China. <sup>3</sup>Institute of Advanced Technology, Westlake Institute for Advanced Study, Hangzhou, Zhejiang Province, China. <sup>4</sup>Westlake Institute for Optoelectronics, Fuyang, Hangzhou, Zhejiang, China. ✉e-mail: [qiumin@westlake.edu.cn](mailto:qiumin@westlake.edu.cn); [yanwei@westlake.edu.cn](mailto:yanwei@westlake.edu.cn)

(SVHP), the anomalous SVHP, the anomalous Hall phase, and the anti-helical edge states. All designs are based on the inherent coupling between the AM modes using micro-ring resonators on SOI platform. They do not require auxiliary coupling components, optical non-linearity or time-reversal symmetry breaking.

## Results

### Coupling winding number

Modes in nearby resonators exchange their energy through evanescent coupling. This coupling phenomenon is abstracted into a complex-valued coupling coefficient, denoted by  $t = |t|e^{i\phi}$ . The inverse of  $|t|$  refers to the time scale required for the energy exchange, while  $\phi$  specifies the phase imparted to the mode through the coupling. The  $t$  parameter depends on the relative positions of the resonators. Although this dependence can take various specific forms, it is possible to extract global characteristics. Considering one resonator ( $B$ ) evolving around the other ( $A$ ) along an arbitrary closed path  $\mathcal{S}$  [Fig. 1a], the coupling coefficient  $t$  simultaneously traces a closed trajectory  $\gamma$  in the complex plane. Consequently, a homotopy invariant  $\pi_1(S^1)^{35}$  can be defined for the mapping  $\mathcal{S} \rightarrow \gamma$ , which quantifies how many times the complex  $t$  counterclockwise encircles the origin as resonator  $B$  completes one counterclockwise loop around resonator  $A$ . In other words, it represents the net number of times that the phase of the coupling coefficient changes by  $2\pi$ . This topological invariant, referred to as the *coupling winding number*  $W$ , can be conveniently expressed by parametrizing  $\mathcal{S}$  with a relative angle  $\theta \in [0, 2\pi]$  between the  $A$  and  $B$  resonators [see Fig. 1a] as

$$W = \frac{1}{2\pi i} \oint_{\mathcal{S}} d\theta \frac{d}{d\theta} \log[t(\theta)] \quad (1)$$

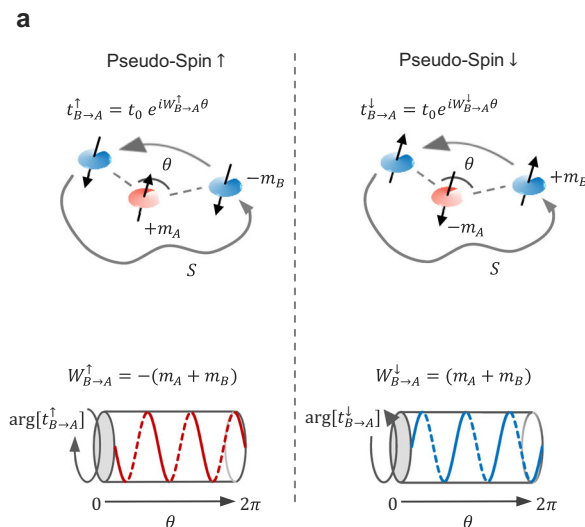
The topological invariant  $W$ , being integer, remains constant under continuous deformations of the modes and evolution path,

except during a topological transition (the change of the inherent topological orders of the modes or the emergence of a new zero in  $t$  on the path  $\mathcal{S}$ , see Supplementary Sec. 8.1 for detailed derivations).

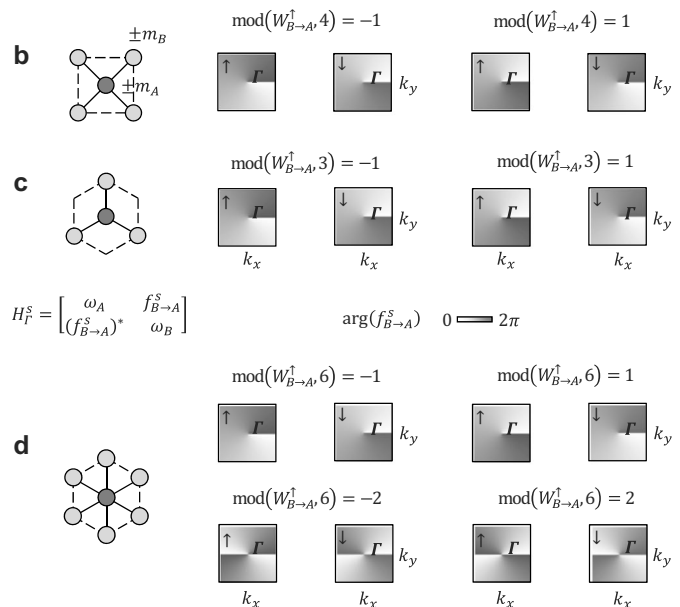
To further solidify the meaning of the coupling winding number and to connect it to our topic of interest regarding pseudo-spin-derived topological phases, we investigate coupling between optical resonators with continuous rotational symmetry about parallel axes, e.g., micro-ring resonators on planar substrates. Supported optical resonance modes  $\mathbf{E}_m(\mathbf{r}) = \mathbf{e}_m(\rho, z) \exp(im\phi)$  ( $\rho, \phi, z$  are the cylindrical coordinates) are classified by their angular-momentum (AM) quantum numbers  $m = \dots, -1, 0, 1, \dots$ , which summarize both spin and orbital components. Consider a pair of such coupled resonators (labeled by  $A$  and  $B$ ), which support degenerate AM modes  $\pm m_A$  and  $\pm m_B$  ( $m_A, m_B > 0$ ), respectively, within the frequency range of interest. The coupling between two modes with opposite-sign AM numbers in two resonators is more efficient than that between the modes with the same-sign AM numbers, due to better momentum matching in the former case. Particularly, when  $m_A + m_B \gg |m_A - m_B|$  (that requires high AM numbers,  $m_A, m_B \gg 1$ , with magnitudes close to each other), the coupling between the same-sign AM modes is substantially suppressed and can be neglected (see supplementary Fig. 1 for numerical validations). In this case, only the coupling between the  $m_A$  and  $-m_B$  modes, and its time reversal ( $\mathcal{T}$ ) symmetric counterpart between the  $-m_A$  and  $m_B$  modes need to be considered, thus suggesting the following pseudo-spins [Fig. 1a]:

$$\uparrow \equiv \{m_A, -m_B\} \text{ and } \downarrow \equiv \{-m_A, m_B\} \quad (2)$$

We then examine the coupling winding numbers  $W$ 's for opposite pseudo-spins with Eq. (1). It is found that the opposite AM numbers in the two pseudo-spins give opposite phase profiles in the electric fields, which further results in the opposite coupling winding numbers for the two pseudo-spins [Fig. 1a; see

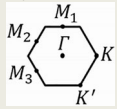
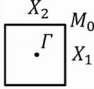
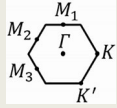


**Fig. 1 | Coupling winding number: definition, pseudo-spin-contrasting characteristics, and  $k$ -space vortices.** **a** Coupling winding number  $W_{B \rightarrow A}$ , a real-space topological invariant, defined by tracing the evolution of the coupling coefficient along a closed path  $S$  (parameterized by the relative angle  $\theta$ ) where one resonator ( $B$ , blue) winds counterclockwise around the other ( $A$ , red). Consider a pair of coupled resonators with continuous rotational symmetry that support modes with angular-momentum quantum numbers  $\pm m_A$  and  $\pm m_B$ , respectively, within the frequency range of interest. The coupling winding numbers assume a simple form



and take opposite values for the opposite pseudo-spins ( $\uparrow, \downarrow$ , see Eq. (2) for the definition). **b–d** Vortices of the  $k$ -space coupling coefficient at the  $\Gamma$  point in the Brillouin zone of  $C_N|_{N=3,4,6}$  crystal, controlled by the coupling winding number. The  $k$ -space coupling term  $f_{B \rightarrow A}^s$  is computed by summarizing up the nearest  $B \rightarrow A$  couplings:  $f_{B \rightarrow A}^s(\mathbf{k}) = \sum_{n=1}^N t_{B \rightarrow A}^s(\theta_n) e^{i\mathbf{k} \cdot \mathbf{a}_n}$  with  $\mathbf{a}_n = a \cos(\theta_n) \hat{x} + a \sin(\theta_n) \hat{y}$ ,  $\theta_n = 2\pi(n-1)/N$ , and  $t_{B \rightarrow A}^s(\theta_n) = t_0 e^{iW_{B \rightarrow A}^s(\theta_n - \theta)}$  with  $t_0$  being a positive real number. Note that once  $W_{B \rightarrow A}^{\uparrow}$  is known,  $W_{B \rightarrow A}^{\downarrow}$  can be inferred from  $W_{B \rightarrow A}^{\downarrow} = -W_{B \rightarrow A}^{\uparrow}$ , so only  $W_{B \rightarrow A}^{\uparrow}$  is indicated in (**b–d**).

**Table 1 | The dependence of  $\chi_{\tau}^s$  [topological charge of  $k$ -space coupling term  $f_{B \rightarrow A}^s(\mathbf{k})$ , cf. Equation (5)] on  $\text{mod}(W_{B \rightarrow A}^s, N)$  for  $C_N$  symmetric crystals**

Crystal	$\text{mod}(m_A + m_B, N)$	$\text{mod}(W_{B \rightarrow A}^s, N)$	$\chi_{\tau}^s$	$\chi_{\mathbf{M}_{0,1,2,3}}^s$	$\chi_{\mathbf{X}_{1,2}}^s$	$\chi_{\mathbf{K}}^s$	$\chi_{\mathbf{K}'}^s$
 $C_3$	0	0	0	0		-1	+1
	1	-s	-s	0		$s\delta_s^{-1}$	$s\delta_s^{-1}$
	-1	+s	+s	0		$-s\delta_s^{-1}$	$-s\delta_s^{-1}$
 $C_4$	0	0	0	0			
	1	-s	-s	+s	0		
	-1	+s	+s	-s	0		
 $C_6$	0	0	0	0		0	0
	1	-s	-s	+s		-s	-s
	-1	+s	+s	-s		+s	+s
	2	-2s	-2s	0		+s	+s
	-2	+2s	+2s	0		-s	-s
3	0	0	0	0		0	0

$\text{mod}(W_{B \rightarrow A}^s, N)$  is the modulus of coupling winding number with respect to rotational symmetry order  $N=3, 4, 6$ . The value range of the  $\text{mod}(W_{B \rightarrow A}^s, N)$  is defined in  $\{[-N/2] + 1, [-N/2] + 2, \dots, [N/2] - 1, [N/2]\}$  and  $[x]$  being the floor function.  $s=1, -1$  correspond to spin  $\uparrow$  and  $\downarrow$ , respectively.  $\delta_n^m = 1$  for  $n=m$ , otherwise  $\delta_n^m = 0$ .  $m_A$  and  $m_B$  are the magnitudes of the AM numbers of the coupled modes. The lattice arrangements in real space are sketched in Fig. 1b-d.

Supplementary Sec. 2 for derivations]:

$$W_{B \rightarrow A}^s = -s(m_A + m_B) \text{ and } W_{A \rightarrow B}^s = -W_{B \rightarrow A}^s, \quad (3)$$

where  $s=1, -1$  correspond to the pseudo-spin  $\uparrow$  and  $\downarrow$ , respectively, and the subscript  $B(A) \rightarrow A$  ( $B$ ) specifies the coupling direction. Hereafter, the pseudo-spin indices  $s=1, -1$  or  $s=\uparrow, \downarrow$  are interchangeably used for convenience. Furthermore, considering that the evolution path  $S$  that defines the winding number is a circle centered at a position-fixed resonator (let's say resonator  $A$ ), and denoting the relative angle between the two resonators by  $\theta$ , it follows that the coupling coefficients take the following forms

$$t_{B \rightarrow A}^s \sim e^{iW_{B \rightarrow A}^s \theta} \text{ and } t_{A \rightarrow B}^s \sim e^{-iW_{B \rightarrow A}^s \theta}, \quad (4)$$

which thus suggest that the phase evolution of the coupling coefficient between AM modes, as a function of the relative position between the resonators, is dictated by the coupling winding number.

### Vortices in the Brillouin zone and summation rule

As a pseudo-spin-contrasting topological invariant, the coupling winding number is expected to find broad applications in pseudo-spin-derived topological physics. To concretize this vision, we establish lattice models by taking the  $A$ - $B$  resonator pair as a lattice element. Further, consider that the lattice has a  $C_N$  (where  $N=3, 4, 6$ ) rotational symmetry with the resonator  $A$  and  $B$  both serving as the rotation center (note that the implementation of the  $C_6$  lattice needs a careful setting, see Supplementary Fig. 3; nevertheless, our subsequent demonstrations mostly focus on the  $C_{3,4}$  lattices). So, around each resonator  $A$ , there are  $N$ 's nearest resonator  $B$ 's at the same distance, and vice versa; only the nearest  $A$ - $B$  coupling is considered.

The Hamiltonians of these crystals consist of diagonal terms  $\omega$ 's—the uncoupled resonant frequencies—, and off-diagonal terms  $f(\mathbf{k})$ 's—the summation of the nearest  $A$ - $B$  couplings. The band topology is governed by the coupling terms  $f(\mathbf{k})$ 's. The participation of  $W$  in  $A$ - $B$  couplings [Eq. (4)], and consequently in  $f(\mathbf{k})$ 's, introduce a new DOF for band engineering. Due to the discretized angles  $\theta_n = 2\pi(n-1)/N$  ( $n=1, 2, 3, \dots$ ) between the nearest  $A$  and  $B$  resonators in these  $C_N$  lattices, different  $W$ 's sharing the same remainder modulo  $N$ , denoted

by  $\text{mod}(W, N)$  for abbreviation, are equivalent in  $f(\mathbf{k})$ 's, due to the same phase profiles of the real-space coupling coefficient [Eq. (4)]. The systems can thus be classified, examined according to the different values of  $\text{mod}(W, N)$  with the value range defined in  $\{[-N/2] + 1, \dots, [N/2] - 1, [N/2]\}$  and  $[x]$  being the floor function.

We then demonstrate that certain values of  $\text{mod}(W, N)$  give rise to vortices of  $f(\mathbf{k})$ 's [see Table 1 and Fig. 1b-d] at high-symmetric points in the Brillouin zone. Such high-symmetric points, denoted by  $\tau$ , are the  $\Gamma, \mathbf{M}$  and  $\mathbf{X}$  points for the  $C_4$  lattice, and the  $\Gamma, \mathbf{K}, \mathbf{K}'$  and  $\mathbf{M}$  points for the  $C_3$  and  $C_6$  lattices. Only at these specific  $\tau$ 's can these vortices exist. Near the vortices, the coupling terms  $f(\mathbf{k})$ 's take the leading-order expressions:

$$f_{B \rightarrow A}^s(\mathbf{k}) \sim \delta k^{|\chi_{\tau}^s|} e^{i\chi_{\tau}^s \theta(\delta \mathbf{k})} \text{ and } f_{A \rightarrow B}^s(\mathbf{k}) \sim \delta k^{|\chi_{\tau}^s|} e^{-i\chi_{\tau}^s \theta(\delta \mathbf{k})}. \quad (5)$$

where  $\delta \mathbf{k} = \mathbf{k} - \tau$ , and  $\theta(\delta \mathbf{k})$  denotes the angle of  $\delta \mathbf{k}$ ;  $\chi_{\tau}^s$  is an integer topological charge of the vortex; the subscript  $B \rightarrow A$  ( $A \rightarrow B$ ) denotes the coupling from the resonator  $B$  ( $A$ ) to  $A$  ( $B$ ). Notably,  $\text{mod}(W, N)$  determines the existence of the vortex as well as its topological charge, as summarized in Table 1 and shown in Fig. 1b-d for representative examples at the  $\Gamma$  point. For example, in the  $C_4$  lattice, only when  $\text{mod}(W_{B \rightarrow A}^s, 4) = \pm 1$ , the vortices can exist at the  $\Gamma$  and  $\mathbf{M}$  points, and their topological charges are  $\chi_{\Gamma}^s = \text{mod}(W_{B \rightarrow A}^s, 4)$  and  $\chi_{\mathbf{M}}^s = -\text{mod}(W_{B \rightarrow A}^s, 4)$ , respectively. Evidently, the opposite values of  $W_{B \rightarrow A}^s$  for the two pseudo-spins transfers into the opposite values of  $\chi_{\tau}^s$  for the two pseudo-spins. Moreover, in the  $C_6$  lattice, the high-order vortices ( $\chi_{\tau}^s = \pm 2$ ) can emerge at the  $\Gamma$  point when  $\text{mod}(W_{B \rightarrow A}^s, 6) = \pm 2$ . For comprehensive information, please refer to Table 1.

It is noticed that in Table 1, for each pseudo-spin, the total topological charge of the coupling terms  $f(\mathbf{k})$ 's at all high-symmetric points is

$$\sum_{\tau} \chi_{\tau}^s = 0, \quad (6)$$

This can be interpreted from Hopf-Poincaré theorem, which states that the global topological charge of a complex function (viewed as 2D vector fields) on a compact orientable manifold  $M$  is equal to  $M$ 's Euler characteristic. A 2D Brillouin zone, i.e.,  $T^2$ , has a zero Euler characteristic. Given that the  $\mathbf{k}$ -space vortices only exist at high-

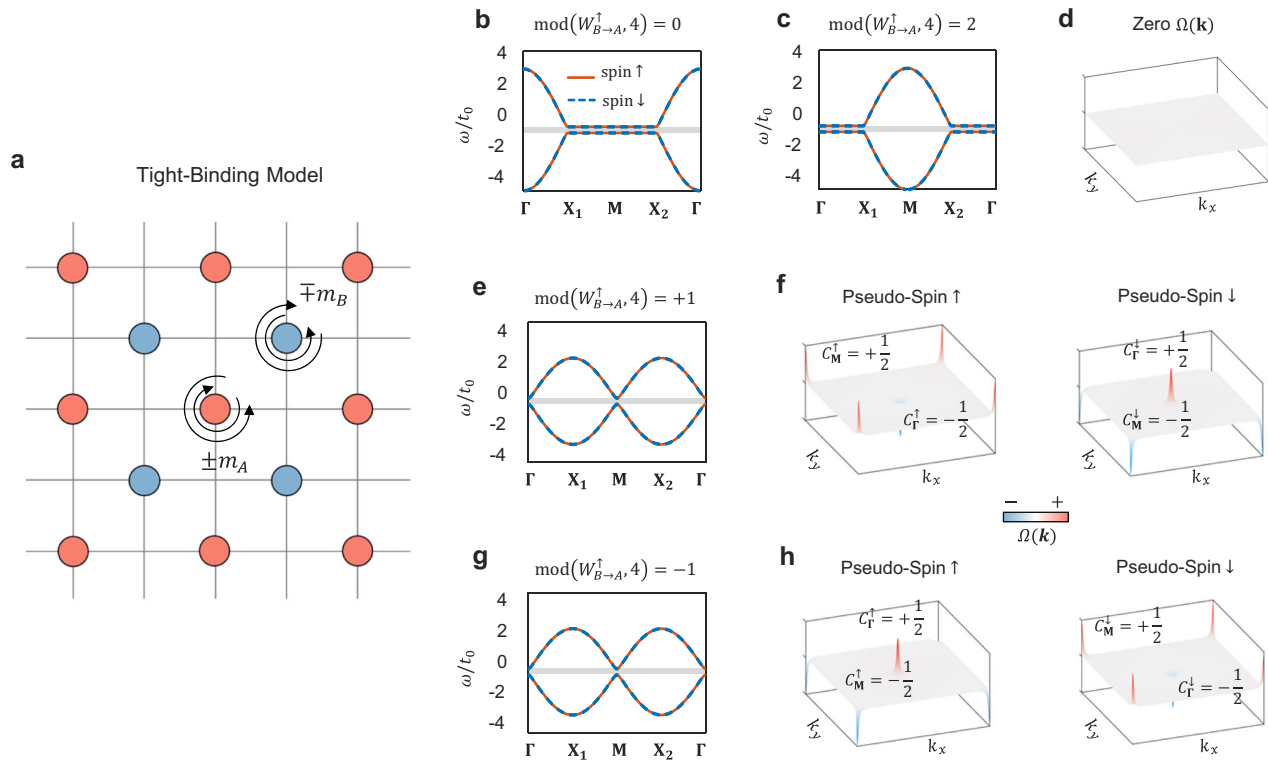


**Fig. 2 | Spin-valley Hall phases realized in 4-fold rotational symmetric square lattices.** **a** Sketch of a 4-fold rotational symmetric ( $C_4$ ) lattice consisting of coupled resonator  $A$  (red) and  $B$  (blue). The modes supported are labeled by their AM numbers,  $\pm m_A$  and  $\pm m_B$ . **b–h.** Band diagrams, and Berry-curvature  $\Omega(\mathbf{k})$  distributions of valence bands across the Brillouin zone, obtained by tight-binding model (TBM) simulations for various values of  $\text{mod}(W_{B \rightarrow A}^\dagger, 4)$ . When  $\text{mod}(W_{B \rightarrow A}^\dagger, 4) = 0$ , the Berry curvature vanishes and the bands are trivial. When

$\text{mod}(W_{B \rightarrow A}^\dagger, 4) = \pm 1$ , the special Berry-curvature distributions, together with indicated spin-valley Chern numbers, evidence the SVHP. In the TBM simulations, the resonant frequencies of the  $\pm m_A$  and  $\pm m_B$  modes are set to be  $0.2t_0$  and  $-0.2t_0$ , respectively, and accordingly the energy difference between the modes is  $\Delta = \omega_A - \omega_B = 0.4t_0$ , where  $t_0$  denotes the coupling strength; only the nearest  $A$ – $B$  coupling is considered.

symmetric  $\tau$  points in  $C_N$  symmetric systems,  $\sum_\tau \chi_\tau^s$  respects this summation rule.

Intuitively, even without performing band analysis, we envision that, such pseudo-spin-contrasting vorticities in the Brillouin zone, controlled by the coupling winding number, may support a broad range of pseudo-spin-derived topological phases. Below, we shall justify this intuition—showing that these vorticities relate intimately to Dirac cones and topological valleys, and delicately arranging them in the  $\mathbf{k}$  space can induce various pseudo-spin-derived topological phases—, and propose practical designs based on SOI platform.

### Spin-valley Hall phase

We first show the realization of the spin-valley Hall phase (SVHP) in  $C_4$  symmetric square lattices. We focus on  $\text{mod}(W_{B \rightarrow A}^\dagger, 4) = \pm 1$ , since they support the vortices of the  $\mathbf{k}$ -space coupling terms at the  $\Gamma$  and  $\mathbf{M}$  points (Table 1). The leading-order Hamiltonians around the  $\Gamma$  and  $\mathbf{M}$  points are given by

$$H_\tau^s(\delta\mathbf{k}) = 2at_0 d_\tau \left[ \chi_\tau^s \delta k'_x \hat{\sigma}_x - \delta k'_y \hat{\sigma}_y \right] + \frac{\Delta}{2} \hat{\sigma}_z + \frac{\omega_A + \omega_B}{2} \hat{\sigma}_0, \quad (7a)$$

where  $\hat{\sigma}_{x,y,z}$  are the Pauli matrices,  $\hat{\sigma}_0$  is the identity matrix;  $d_\tau = 1, -1$  for the  $\Gamma$  and  $\mathbf{M}$  valleys, respectively;  $\Delta = \omega_A - \omega_B$  with  $\omega_A$  and  $\omega_B$  denoting energies of the  $\pm m_A$  and  $\pm m_B$  modes;  $\delta k'_x \equiv (\delta k_x - \delta k_y)/\sqrt{2}$ ,  $\delta k'_y \equiv (\delta k_x + \delta k_y)/\sqrt{2}$ , and  $\delta \mathbf{k} = \mathbf{k} - \tau = \delta k_x \hat{x} + \delta k_y \hat{y}$ . The eigenstate of  $H_\tau^s$  takes the form  $[A_\tau^s; B_\tau^s]$  with  $A_\tau^s$  and  $B_\tau^s$  referring to the modal amplitudes in the resonator  $A$  and  $B$ , respectively.

When the  $A$ – $B$  detuning vanishes ( $\Delta = 0$ ), the Hamiltonian is the 2D massless Dirac equation featuring conic bands degenerate at the  $\Gamma$

and  $\mathbf{M}$  points. By symmetry analysis (detailed in Supplementary Sec. 8.2), we identify that the generation of the Dirac cones are protected by  $\mathcal{A}$  symmetry, where  $\mathcal{A} = UK$  represents a joint operator of complex conjugate  $K$  and half lattice translation  $U = \mathbf{a}_1/2 + \mathbf{a}_2/2$  ( $\mathbf{a}_{1,2}$  being lattice vectors), and the localization at  $\Gamma$  and  $\mathbf{M}$  points is protected by  $C_4$  symmetry. When the  $A$ – $B$  detuning is introduced ( $\Delta \neq 0$ ),  $\mathcal{A}$  symmetry is broken, the band degeneracies are lifted, and the valleys (i.e., energy extrema) are formed at the  $\Gamma$  and  $\mathbf{M}$  points. Meanwhile, non-vanishing Berry curvatures are allowed around the  $\Gamma$  and  $\mathbf{M}$  points. The integration of the Berry curvature in the valence band described by the approximated Hamiltonian  $H_\tau^s$  gives the spin-valley Chern number  $C_\tau^s$ , which here reduces to

$$C_\tau^s = -\text{sign}(\Delta) \chi_\tau^s / 2. \quad (7b)$$

Clearly, when either the pseudo-spin ( $s$ ) or valley ( $\tau$ ) index is changed,  $C_\tau^s$  reverses its sign due to the pseudo-spin/valley dependence of  $\chi_\tau^s$ . This signature reproduces that of the SVHP. The SVHP was firstly introduced in the condensed matter systems utilizing anti-ferromagnetic effects in a graphene-like hexagonal lattice<sup>36</sup>, and, later, was theoretically revisited in photonics by leveraging optical nonlinearity<sup>27</sup>. Both strategies require time-reversal symmetry ( $\mathcal{T}$ ) breaking to induce spin/pseudo-spin-contrasting mass terms. Utilizing the coupling winding number that gives a pseudo-spin-contrasting momentum prefactor  $\chi_\tau^s$  in the Hamiltonian [Eq. (7a)], we circumvent the challenging  $\mathcal{T}$ -breaking requirement and go beyond the anti-ferromagnetic model.

Figure 2 validates the predicted SVHP with the tight-binding model (TBM) simulations [see the caption for simulation details]. It is

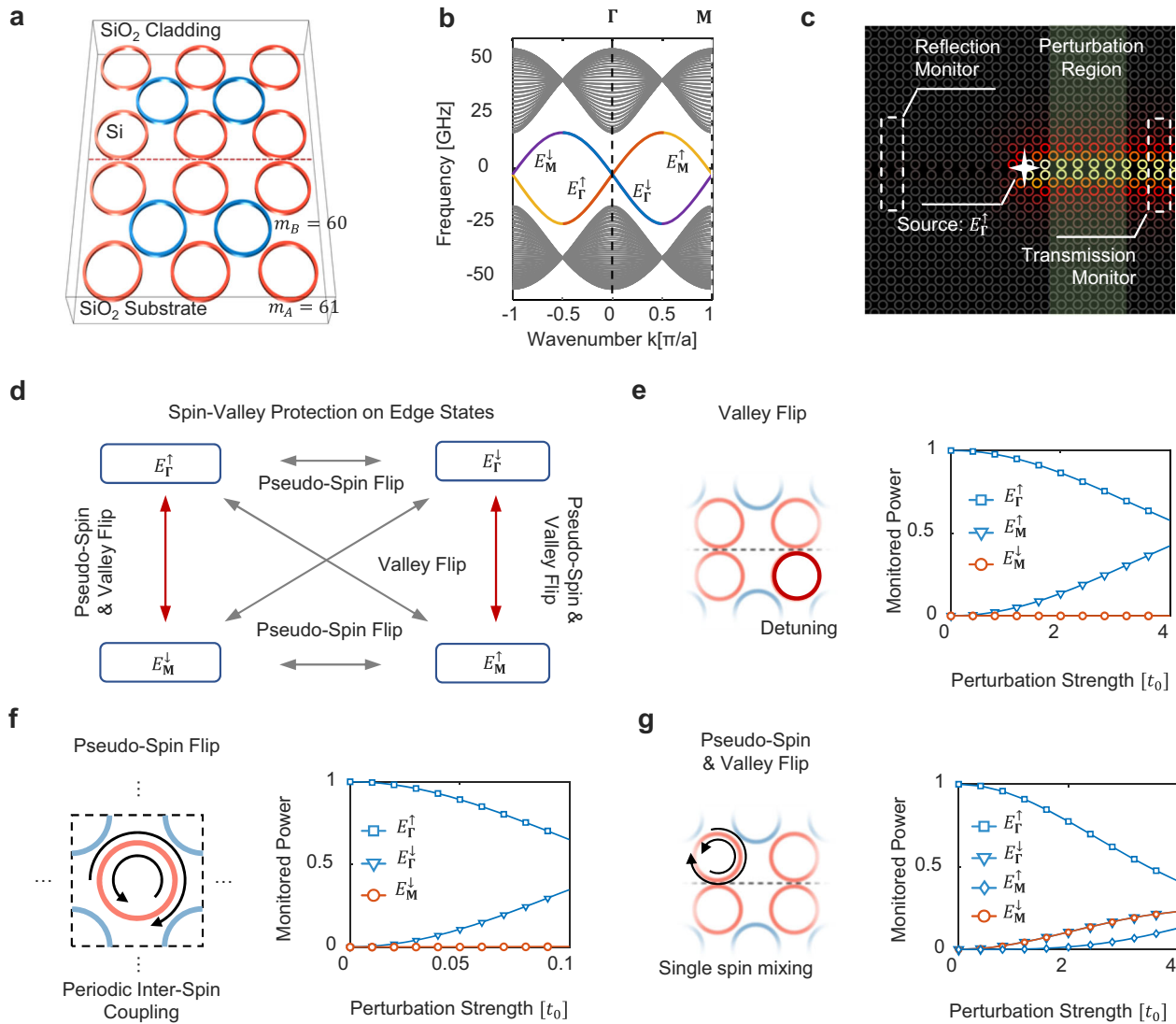


**Fig. 3 | Photonic implementation of a spin-valley Hall phase based on silicon-on-insulator platform.** **a** Sketch of a spin-valley Hall phase (SVHP) design by using Si microring resonators (MRRs) on a SiO<sub>2</sub> substrate with a SiO<sub>2</sub> cladding. The outer radii of MRR A (red) and B (blue) are 6.45 μm and 6.35 μm; both are 500 nm wide and 220 nm high; the gap distance between the MRR A and B is 250 nm. TE-polarized AM modes with  $m_A = 61$  at  $\lambda_A = 1546.7$  nm, and  $m_B = 60$  at  $\lambda_B = 1546.9$  nm are supported, giving  $\text{mod}(W_{B \rightarrow A}^\dagger, 4) = -1$ . **b** Projected band diagram of an interface between two adjacent SVHP copies. The gap distance between the MRRs across the interface [see the dashed line in **a**] is 150 nm. The band frequency is offset by the central frequency of the involved modes, corresponding to a wavelength of  $\lambda_A/2 + \lambda_B/2 = 1546.8$  nm. The pseudo-spin index of the lower SVHP system

in **a** is used to label the pseudo-spin configuration of the entire system. **c** Sketch of simulation setting for examining transport properties of ESs. A perturbation region that potentially induces pseudo-spin/valley flipping is included. **d** Graphical representation of transitions between edge states (ESs) with two pseudo-spin DOFs and two valley DOFs induced by various perturbations. **e-g**, Normalized power distributions of ESs after scatterings of valley flipping (**e**), pseudo-spin flipping (**f**) and both pseudo-spin and valley flipping (**g**) [see Supplementary Fig. 4 for detailed information of defect settings]. The perturbation strength is normalized by the  $A$ - $B$  coupling strength  $t_0 = 18.6$  GHz. The incident ES is set to  $E_\Gamma^\dagger$ , the other three ESs  $E_\Gamma^\dagger$ ,  $E_M^\dagger$ ,  $E_M^\dagger$  are induced by the defects.

observed that, when  $\text{mod}(W_{B \rightarrow A}^\dagger, 4) = \pm 1$  and an energy detuning between the modes A and B is introduced, the Berry curvatures and their integrated spin-valley Chern numbers  $C_2^s$  show the characteristics of the SVHP. On the other hand, when  $\text{mod}(W_{B \rightarrow A}^\dagger, 4) = 0, 2$ , the bands are topologically trivial. As examined in Supplementary Sec. 9, since the moderate  $C_4$  symmetry breaking only move the Dirac cones/valleys from the high symmetric points instead of eliminate them, this SVHP possesses a degree of robustness against lattice deformation.

We design a photonic SVHP based on SOI platform. As is shown in Fig. 3a, a square unit cell is composed of a pair of Si micro-ring-resonator (MRR) A (red) and B (blue) with width 500 nm, height 220 nm, gap distance 250 nm, and outer radii  $r_A = 6.45 \mu\text{m}$  and  $r_B = 6.35 \mu\text{m}$ ; both the substrate and the cladding are composed of SiO<sub>2</sub>;  $n_{\text{Si}} = 3.45$  and  $n_{\text{SiO}_2} = 1.44$  (refractive index). By performing modal analysis with

COMSOL Multiphysics, we identify that the MRR A and B support TE-polarized AM modes with  $m_A = 61$  at  $\lambda_A = 1546.7$  nm and  $m_B = 60$  at  $\lambda_B = 1546.9$  nm, respectively. This gives  $\text{mod}(W_{B \rightarrow A}^\dagger, 4) = -1$  [Eq. (3)]. Accordingly, the valley-Chern numbers of the designed SVHP are  $C_2^s = \pm s/2$  and  $C_2^M = \mp s/2$  [Eq. (7b)]; note  $\Delta > 0$ . Further, to generate the kink edge states (ESs), we interface two identical SVHP copies. Across the interface, the same-type MRRs are coupled [Fig. 3a], which results in the coupling between the opposite pseudo-spins in the upper and lower regions of the interface. For convenience of description, we use the pseudo-spin index of the lower region to label the pseudo-spin configuration of the entire system. The changes in the spin-valley Chern numbers between the valence bands in the lower and upper regions of the interface are  $\Delta C_2^s = \pm s$  and  $\Delta C_2^M = \mp s$ , the magnitude of which determines the number of the ESs, while the sign of which indicates the

propagation direction of the ESs. It predicts a total of four-channel ESs corresponding to two pseudo-spin DOFs and two pseudo-valley DOFs. Specifically, for a fixed valley or pseudo-spin index, the ESs of the opposite pseudo-spin or valley index propagate in opposite directions. Figure 3b plots the projected band diagram of the interface (the gap distance between the MRR  $A$ 's across the interface is 150 nm; see Supplementary Sec. 3 for the simulation method that combines the TBM and the finite element method). It shows that the ESs emerge inside the bandgap, and their properties are well characterized by  $\Delta C_{\Gamma, M}^s$ , as expected.

The unique feature of the SVHP give the ESs an exotic character [Fig. 3d]: neither pseudo-spin- nor valley-flipping defects can efficiently induce transitions between the same-direction ESs that exhibit the opposite pseudo-spin and valley indices. So, to allow such transitions, defects, capable of flipping both pseudo-spin and valley indices, are needed, thus suggesting a two-fold pseudo-spin-valley protection. To validate this, we examine transport properties of the ESs against defects [Fig. 3c]. Three types of the defects—inducing valley flipping, pseudo-spin flipping, and pseudo-spin & valley flipping—are considered; their settings are sketched in Supplementary Fig. 4. Figure 3e–g plot the normalized power distributions of the ESs as functions of perturbation strengths. The initially excited ES is set to  $E_{\Gamma}^{\uparrow}$  (an edge state at the  $\Gamma$  valley with the pseudo-spin  $\uparrow$ ), and the other three ESs  $E_{\Gamma}^{\downarrow}$ ,  $E_{\mathbf{M}}^{\uparrow}$ ,  $E_{\mathbf{M}}^{\downarrow}$  are induced by the defects. It shows that the valley-flipping defect only induces the transitions between  $E_{\Gamma}^{\uparrow}$  and  $E_{\mathbf{M}}^{\uparrow}$  [Fig. 3e], while the other transition channels are forbidden due to the pseudo-spin protection. On the other hand, the pseudo-spin-flipping defect primarily induces the transitions between  $E_{\Gamma}^{\uparrow}$  and  $E_{\Gamma}^{\downarrow}$ , while the transitions between  $E_{\Gamma}^{\uparrow}$  and  $E_{\mathbf{M}}^{\downarrow}$  are suppressed due to the valley protection. Note that when the pseudo-spin-flipping perturbation strength reaches  $\sim 0.1t_0$  ( $t_0 = 18.6$  GHz, coupling strength between the nearest MRR  $A$  and  $B$ ), the power of the excited  $E_{\mathbf{M}}^{\downarrow}$  is only about 3 orders of magnitude lower than the incident power [Fig. 3f]. The transitions between  $E_{\Gamma}^{\uparrow}$  and  $E_{\mathbf{M}}^{\downarrow}$  only become noticeable when the pseudo-spin-valley flipping defect occurs [Fig. 3g]. These results confirm that the pseudo-spin-valley protection suppresses the transitions between the ESs of the opposite pseudo-spin and valley indices under defects that induce valley or pseudo-spin flipping.

### Anomalous spin-valley Hall phase

We next show the realization of a variant of the SVHP—named anomalous spin-valley Hall phase (aSVHP)—in  $C_3$  symmetric triangle lattices. By examining the band Hamiltonian around the high-symmetric points, we observe that the spin-valley Chern number is also given by Eq. (7b) as for the  $C_4$  lattices. Nevertheless, the involving of two pseudo-spin DOFs and three valley DOFs at the  $\Gamma$ ,  $\mathbf{K}$ , and  $\mathbf{K}'$  points, results in an unusual topological pattern different from the SVHP. Specifically, the aSVHP occurs when  $\text{mod}(W_{\mathbf{B} \rightarrow \mathbf{A}}^{\uparrow}, 3) = \pm 1$ . By referring to Eq. 1 and Eq. (7b), we observe that, when  $\text{mod}(W_{\mathbf{B} \rightarrow \mathbf{A}}^{\uparrow}, 3) = -1$  [similarly for  $\text{mod}(W_{\mathbf{B} \rightarrow \mathbf{A}}^{\uparrow}, 3) = 1$ ], the  $\Gamma$  and  $\mathbf{K}$  valleys show the opposite spin-valley Chern numbers with  $C_{\Gamma}^{\uparrow} = -C_{\mathbf{K}}^{\uparrow} = \text{sign}(\Delta)/2$  for the pseudo-spin  $\uparrow$ . Flipping the pseudo-spin with  $\text{mod}(W_{\mathbf{B} \rightarrow \mathbf{A}}^{\downarrow}, 3) = 1$ , there are  $C_{\Gamma}^{\downarrow} = -C_{\mathbf{K}}^{\downarrow} = -\text{sign}(\Delta)/2$ . Clearly,  $C_{\Gamma}^{\uparrow} = -C_{\Gamma}^{\downarrow}$  and  $C_{\mathbf{K}}^{\uparrow} = -C_{\mathbf{K}}^{\downarrow}$ . These features are similar to the SVHP, except a time-reversal switching between the  $\mathbf{K}$  and  $\mathbf{K}'$  valleys under the flipping of the pseudo-spins. On the other hand, when  $\text{mod}(W_{\mathbf{A} \rightarrow \mathbf{B}}^{\uparrow}, 3) = 0$ , the  $\mathbf{K}$  and  $\mathbf{K}'$  valleys exhibit pseudo-spin-insensitive valley Chern numbers. This phase corresponds to the valley Hall phase. The above predictions are validated with TBM simulations shown in Fig. 4a–g.

We design a photonic aSVHP using the same settings as those of the SVHP design in Fig. 3, except that the aSVHP here is  $C_3$  symmetric [Fig. 4h]. The AM numbers of the used modes ( $m_A = 61$  and  $m_B = 60$ , cf. Figure 3) indicate  $\text{mod}(W_{\mathbf{B} \rightarrow \mathbf{A}}^{\uparrow}, 3) = -1$ . This gives  $C_{\Gamma}^{\uparrow} = \pm s/2$ ,  $C_{\mathbf{K}}^{\uparrow} = -1/2$  and  $C_{\mathbf{K}}^{\downarrow} = 1/2$  according to Eq. (7b). Further, to generate the kind

ESs, two aSVHP systems (with the MRR  $A$  and  $B$  swapping their positions) are interfaced along the zig-zag direction [Fig. 4h]. The projected band diagram of the interface is plotted in the left panel of Fig. 4i. The four channels of the ESs corresponding to the two pseudo-spin and three valley DOFs appear in the bandgap. Specifically,  $E_{\Gamma}^{\uparrow}$  and  $E_{\mathbf{K}}^{\downarrow}$  propagate to the right along the interface, while  $E_{\Gamma}^{\downarrow}$  and  $E_{\mathbf{K}}^{\uparrow}$  propagate to the left. In addition to the combined pseudo-spin-valley protection as discussed in Fig. 3e–h, the valley protection alone ensures a perfect transmission of the ESs through a sharp bending formed by the zig-zag interfaces<sup>37</sup>. As is shown in the right panel of Fig. 4i, the transmittance of the ESs across a Z-shaped bending approaches almost 100% in the entire spectral range of the ESs. This is further confirmed in Fig. 4j by examining the simulated field distribution (where the incident ES is chosen to  $E_{\Gamma}^{\uparrow}$ ).

### Anomalous Hall phase

For both the SVHP and aSVHP studied above, the band Chern number for one pseudo-spin is consistently zero, i.e.,  $C^s \equiv \sum_{\tau} C_{\tau}^s = 0$ . This result is related to the lattice architecture. First, the use of the  $A$ - $B$  resonator pair in the lattice construction results in a linear relation between  $\chi_{\tau}^s$  (the topological charge of the  $k$ -space coupling coefficient) and  $C_{\tau}^s$  (the spin-valley Chern number) [Eq. (7b)]. Second, the Hopf-Poincaré theorem ensures  $\sum_{\tau} \chi_{\tau}^s = 0$ , which, together with the linear relation between  $\chi_{\tau}^s$  and  $C_{\tau}^s$ , locks  $C^s = 0$ . Therefore, to achieve a non-zero  $C^s$ , it is essential to move beyond the strategy of using a single type of the  $A$ - $B$  resonator pair.

Figure 5 illustrates a simple strategy for realizing anomalous Hall phases (aHPs) with non-zero band Chern numbers. This is achieved by stitching two-types of resonator pairs. As is shown in Fig. 5a, we consider  $A$  (red)- $B$  (blue) and  $C$  (gray)- $B$  resonator pairs, and the two pairs share the same resonator  $B$ . The coupling winding numbers of the two pairs can be assigned different values, offering greater flexibility for manipulating topology. For exemplifications, we stitch the two pairs to form a  $C_4$  symmetric lattice. By referring to the TBM simulations, we enumerate all possible combinations of the coupling winding numbers of the two resonator pairs, and analyze the band topology. It is observed that, the aHPs emerge when  $\text{mod}(W_{\mathbf{B} \rightarrow \mathbf{A}}^{\uparrow} + W_{\mathbf{B} \rightarrow \mathbf{C}}^{\uparrow}, 4) = \pm 1$ , otherwise, there are the SVHPs or the trivial phases with zero band Chern numbers. The relations between the combinations of the coupling winding numbers and the induced topological phases are summarized in the right panel of Fig. 5a. As examined in Supplementary Sec. 9, the non-trivial phases can be maintained even when the  $C_4$  symmetry is broken.

As a proof of this strategy, we design a photonic aHP based on SOI platform. The outer radii of the Si MRR  $A$ ,  $B$  and  $C$  are set to  $r_A = 5.55 \mu\text{m}$  and  $r_B = r_C = 5.45 \mu\text{m}$ , and the gap distances between the nearest  $A$ - $B$  MRRs and  $A$ - $C$  MRRs are set to 100 nm and 200 nm, respectively. The other parameters remain the same as those in Figs. 3 and 4. From the modal simulations, we identify that these MRRs support the TE-polarized AM modes with  $m_A = 53$  at  $\lambda_A = 1531.7$  nm and  $m_{B,C} = 52$  at  $\lambda_{B,C} = 1531.7$  nm, respectively. This thus gives  $\text{mod}(W_{\mathbf{B} \rightarrow \mathbf{A}}^{\uparrow} + W_{\mathbf{B} \rightarrow \mathbf{C}}^{\uparrow}, 4) = -1$ . The coupling between the modes leads to four bands for each pseudo-spin, as shown in Fig. 5b. Specifically, the two middle bands connecting to each other have the band Chern number  $C^s = -2s$  [pseudo-spin index is given by that of the resonator pair  $A$ - $B$  defined in Eq. (2)], while the bottom and top bands, separated from the middle bands, share the same band Chern number  $C^s = s$ . The non-zero band Chern numbers and the vanishing gauge flux—verified by summarizing the phase shift of the coupling coefficient along the boundary of the unit cell in real space and finding a zero value—suggest that the topological phase is indeed an aHP<sup>21</sup>. This specific gauge distribution arises from the coupling winding number, revealing another utility of this concept (see Supplementary Sec. 10 for a detailed discussion).

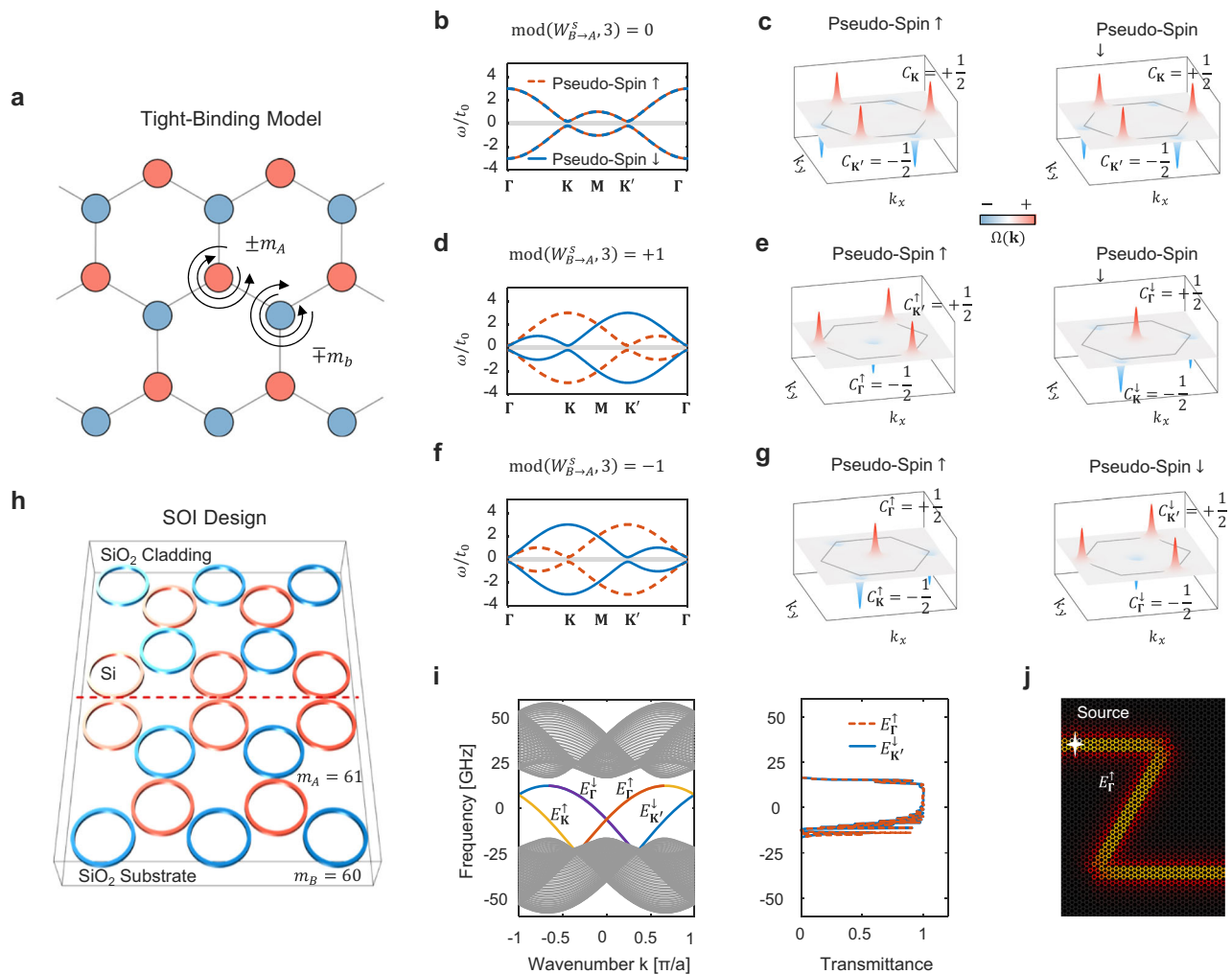


**Fig. 4 | Anomalous spin-valley Hall phase realized in 3-fold rotational symmetric triangle lattices and its photonic design based on silicon-on-insulator platform.** **a** Sketch of a  $C_3$  symmetric lattice consisting of coupled resonator  $A$  (red) and  $B$  (blue). **b–g**, Band diagrams and Berry-curvature  $\Omega(\mathbf{k})$  distributions obtained with TBM simulations for various  $\text{mod}(W_{B \rightarrow A}^s, 3)$ . The valley Hall phase emerges when  $\text{mod}(W_{B \rightarrow A}^s, 3) = 0$ , while the anomalous spin-valley Hall phase (aSVHP) emerges when  $\text{mod}(W_{B \rightarrow A}^s, 3) = \pm 1$ . The TBM simulations use the same parameters as those in Fig. 2. **h** Sketch of a photonic aSVHP based on SOI platform. **i** Projected band diagram of an interface between two adjacent aSVHP systems.

Four channels of the edge states (ESs)  $E_{\Gamma}^{\uparrow}, E_{\Gamma}^{\downarrow}, E_{\mathbf{K}}^{\uparrow}, E_{\mathbf{K}'}^{\downarrow}$ , emerge inside the bandgap. The transmittance spectra of the ESs through a Z-shaped bending are plotted in the right panel. The pseudo-spin index of the lower aSVHP system in **h** is used to label the pseudo-spin configuration of the entire system. **j** Field distributions of an ES passing through a Z-shaped bending. The incident ES is  $E_{\Gamma}^{\uparrow}$  with pseudo-spin  $\uparrow$  and wavenumber at the projected  $\Gamma$  point. In **h–j**, nanophotonic structures used, including Si MRRs and SiO<sub>2</sub> substrates and claddings, utilize the same parameters as those in Fig. 3. The frequency is offset by the central frequency of the involved modes.

Further, to examine the ESs emerged at the interfaces of an aHP slab, we terminate the PhC such that the  $B$ -type MRRs are located at the interfaces. The projected band diagram of the interface is plotted in the left panel of Fig. 5c. It shows that counter-propagating gapless ESs locked with opposite pseudo-spins appear inside the topological bandgaps. These aHP-protected ESs propagate unidirectionally as long as defects do not mix the pseudo-spins. This topological protection is verified by simulations where the ESs encounter random defects created by removing the MRRs near the boundary. Figure 5d and e plot the field distributions, evidencing that the ESs navigate these defects without inducing reflections. This is further confirmed by the simulated transmission spectra shown in the right panel of Fig. 5c. We also demonstrate that such aHP system are robust to lattice disorders, such as the random deviations of the MRRs' positions (see Supplementary Sec. 9 for simulations). Moreover, we note that the ESs exhibit a slow-light behavior, characterized by a high group index ( $n_g > 280$ ) with a bandwidth of approximately  $\Delta f \sim 36$  GHz, suggesting the potential application in slow light transport.

### Anti-helical edge states

For a slab of the designed aHP (Fig. 5), each interface supports a pair of counter-propagating pseudo-spin filtered states, with states of one pseudo-spin propagating in the opposite directions at the two parallel interfaces. These states are known as helical edge states. Contrasting to the helical edge states, the anti-helical edge states also exist—as suggested by developments in topological metals—for which each interface supports a pair of counter-propagating pseudo-spin filtered states, but with states of one pseudo-spin propagating in the same directions at the two parallel interfaces (see the rightmost panel in Fig. 6). The concept of the anti-helical edge states originates from the concept of the anti-chiral edge states in a spinless T-symmetry-broken system. The anti-chiral edge states are derived by modifying the Haldane model<sup>38</sup>, and later demonstrated with gyromagnetic photonic crystals<sup>39</sup>. Including spin/pseudo-spin states in time-invariant systems, it is natural to extend the anti-chiral edge states to the anti-helical edge states, similar to how the chiral edge states are extended to the helical edge states. An earlier study provides a photonic design of the anti-

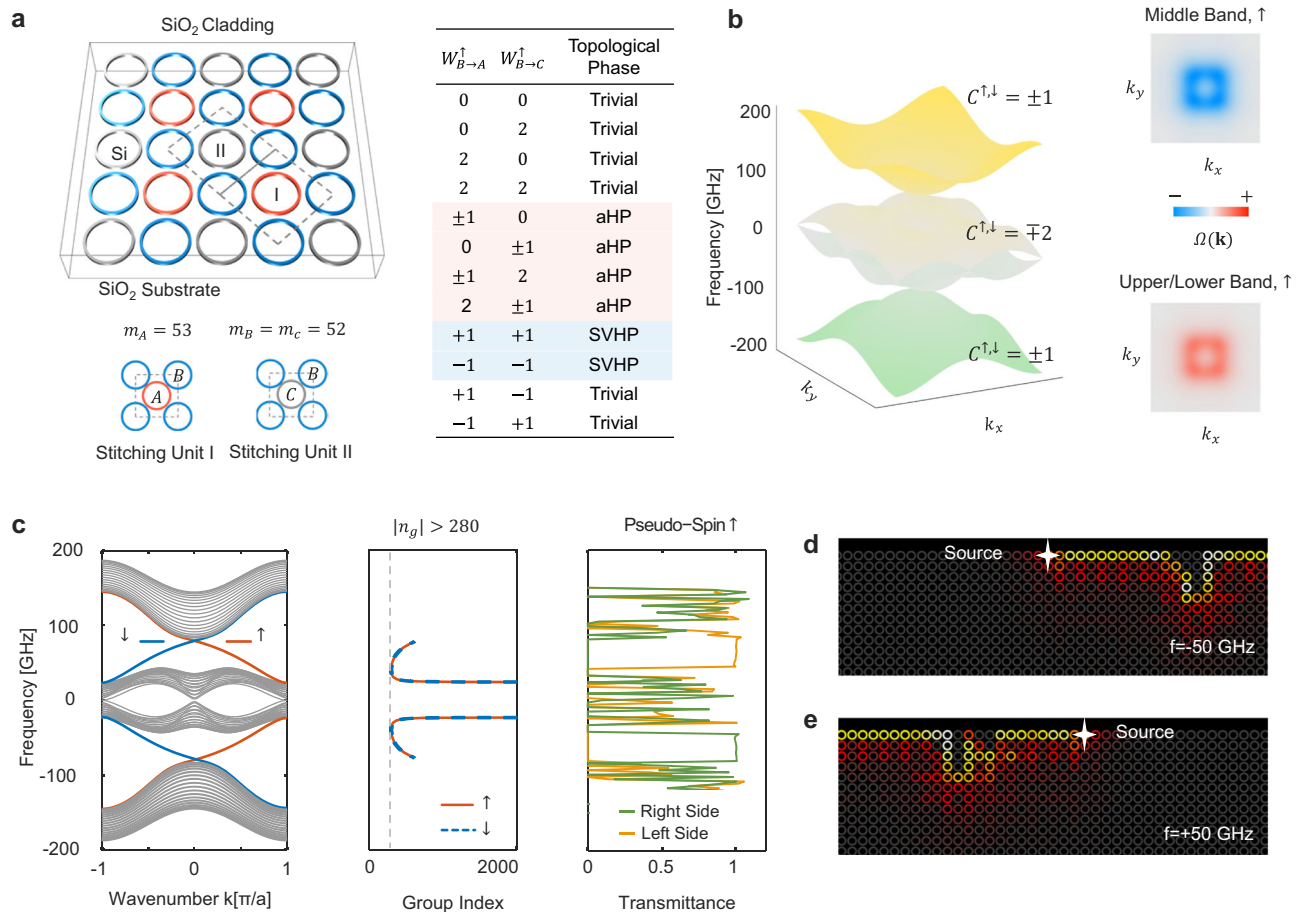


**Fig. 5 | Realization of anomalous Hall phase by stitching coupling winding numbers.** **a** Sketch of the implementation strategy based on stitching two types of resonator pairs in a 4-fold rotational symmetric ( $C_4$ ) square lattice [left panel]. The two stitching units consist of coupled  $A$  (red)- $B$  (blue) and  $C$  (gray)- $B$  MRRs, respectively. Various combinations of the coupling winding numbers of the two-resonator pairs lead to different topological phases, including the anomalous Hall phase (aHP) and the spin-valley Hall phase (SVHP) [right panel]. **b** Bulk band diagram of a designed photonic aHP. The band Chern numbers  $C^s$  are indicated. The outer radii of the MRR  $A$ ,  $B$  and  $C$  are set to  $r_A = 5.55 \mu\text{m}$  and  $r_B = r_C = 5.45 \mu\text{m}$ , with gap distances between the  $A$ - $B$  MRRs and  $A$ - $C$  MRRs being 100 nm and 200 nm, respectively. The other parameters keep the same as those in Figs. 3, 4. The TE-

polarized AM modes with  $m_A = 53$  at  $\lambda_A = 1531.7 \text{ nm}$  and  $m_{B,C} = 52$  at  $\lambda_{B,C} = 1531.7 \text{ nm}$  are supported. The band frequency is offset by the central frequency of the involved modes, i.e.,  $(\lambda_A + \lambda_B + \lambda_C)/3 = 1531.7 \text{ nm}$ . **c** Projected band diagram for an aHP slab [left panel], group index of ESs [middle panel], and transmission spectra of ESs under defects [right panel]. The pseudo-spin indices for the ESs are indicated on the upper interface of the aHP slab. The aHP slab is truncated along the [1 1] direction, so that the MRR  $B$ 's are located at the interfaces. The defects are created by removing MRRs randomly close to the interface. **d, e** Simulated field distributions shows that ESs (pseudo-spin  $\uparrow$ ) detour around defects. The frequencies of the ESs are set to  $f = -50 \text{ GHz}$  (**d**) and  $f = 50 \text{ GHz}$  (**e**).

helical edge states by using auxiliary coupling components to connect both nearest and next-nearest resonators, which is obviously challenging to be implemented<sup>40</sup>. In Supplementary Fig. 5, we provide a simple design of the anti-helical edge states based on the SOI platform based on the concept of the coupling winding number via unitizing intrinsic coupling between AM modes in the nearest MRRs.

## Discussions

Figure 6 summarizes all the topological phases reported in this work that are realized via the coupling winding number. The corresponding designs on the SOI platform are compatible with existing fabrication processes and experimental setups [see Supplementary Sec. 7] and possess a degree of robustness against mode distortion and lattice disorder [see Supplementary Sec. 9]. These simple designs empowered by the coupling winding numbers can facilitate the experimental studies and the applications of these topological phases in photonics. The coupling winding numbers could be further utilized in other types of topological phases, especially the gauge-symmetry-enriched topological phases<sup>41–44</sup>, due to the ability to generate gauge-flux distributions [see Supplementary Sec. 10]. Moreover, the coupling

winding number defined in angle-parameter space can be generalized, e.g., to the lattice space, in intuitively interpreting a wider range of topological phases, such as quantum Hall phase [see Supplementary Sec. 10].

In conclusion, we report a versatile framework for realizing pseudo-spin-derived topological phases based on a central concept—coupling winding number. The coupling winding number characterizes topology of evanescent coupling between nearby resonators, and show opposite values for pseudo-spins in coupled angular-momentum modes. By tailoring the coupling winding number in rotational symmetric photonic crystals, a broad range pseudo-spin-derived topological phases—including the spin-valley Hall phase, the anomalous spin-valley Hall phase, the anomalous Hall phase, and the anti-helical edge states—are implemented based on SOI platform (see Fig. 6 for a summary). The designs leverage the inherent coupling between the AM modes without the need for auxiliary coupling components, breaking time-reversal symmetry, or optical nonlinearity. The versatility and simplicity of the framework suggest its potential for deploying various topological phases in photonics and realizing related applications, particular in robust light transport.

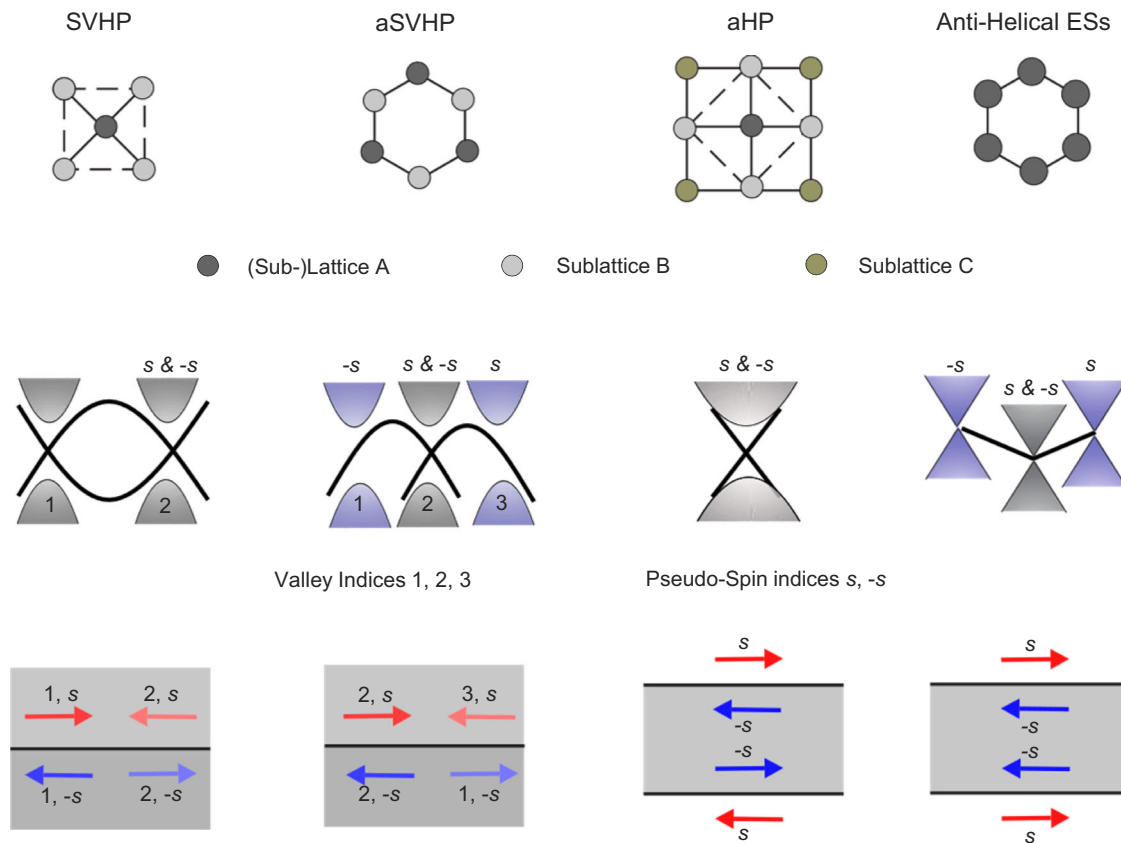


**Fig. 6 | Summary of exemplified pseudo-spin-derived topological structures realized with the concept of the coupling winding number.** Spin-valley Hall phase (SVHP), anomalous spin-valley Hall phase (aSVHP), anomalous Hall phase

(aHP) and anti-helical edge states are demonstrated. Their lattices, band diagrams and the edge-state propagation are sketched. Further details of the photonic designs are provided in Figs. 3–5 and Supplementary Fig. 5, respectively.

Besides, the  $\mathbf{k}$ -space vortices of the inter-coupling terms in Hamiltonians induced by the coupling winding number might hold the potential in generating vortex beams by coupling resonant modes to outgoing radiation fields. Furthermore, given the widespread presence of the coupling winding number across different physical systems, we envision that the present findings may provide useful insights beyond optics and could be extended to other physical systems, such as electronic orbitals and acoustic vibrations.

## Methods

The band diagrams and edge-state transmission spectra were computed using a hybrid approach that combines the finite-element method (FEM) and the tight-binding model (TBM), which reduces computational cost while maintaining predictive accuracy. In this approach, the eigenfrequencies of individual resonators and their inter-coupling coefficients were extracted from three-dimensional FEM simulations performed in COMSOL Multiphysics. These parameters were then used to construct the TBMs, whereby the Maxwell equations were reduced to the corresponding Hamiltonian in a matrix formulation. The implementation details and the effectiveness of this approach are discussed in Section 3 of the Supplementary Materials.

## Data availability

All data supporting this study were obtained from numerical calculations. These data can be fully reproduced using the methods, parameter settings, and simulation configurations described in this article and the Supplementary Material.

## Code availability

The finite-element simulations were performed using commercial software COMSOL Multiphysics. The construction and solution of the tight-binding models follow standard procedures detailed in this article and the Supplementary Material. All scripts used for the tight-binding calculations are available from the authors upon request.

## References

- Lu, L., Joannopoulos, J. D. & Soljačić, M. Topological photonics. *Nat. Photonics* **8**, 821–829 (2014).
- Ozawa, T. et al. Topological photonics. *Rev. Mod. Phys.* **91**, 015006 (2019).
- Hasan, M. Z. & Kane, C. L. Colloquium: topological insulators. *Rev. Mod. Phys.* **82**, 3045–3067 (2010).
- Qi, X.-L. & Zhang, S.-C. Topological insulators and superconductors. *Rev. Mod. Phys.* **83**, 1057–1110 (2011).
- Haldane, F. D. M. & Raghu, S. Possible realization of directional optical waveguides in photonic crystals with broken time-reversal symmetry. *Phys. Rev. Lett.* **100**, 013904 (2008).
- Raghu, S. & Haldane, F. D. M. Analogs of quantum-Hall-effect edge states in photonic crystals. *Phys. Rev. A* **78**, 033834 (2008).
- Wang, Z., Chong, Y. D., Joannopoulos, J. D. & Soljačić, M. Reflection-free one-way edge modes in a gyromagnetic photonic crystal. *Phys. Rev. Lett.* **100**, 013905 (2008).
- Wang, Z., Chong, Y., Joannopoulos, J. D. & Soljačić, M. Observation of unidirectional backscattering-immune topological electromagnetic states. *Nature* **461**, 772–775 (2009).
- Hatsugai, Y. Chern number and edge states in the integer quantum Hall effect. *Phys. Rev. Lett.* **71**, 3697–3700 (1993).

10. Mong, R. S. K. & Shivamoggi, V. Edge states and the bulk-boundary correspondence in Dirac Hamiltonians. *Phys. Rev. B* **83**, 125109 (2011).
11. Staude, I. & Schilling, J. Metamaterial-inspired silicon nanophotonics. *Nat. Photonics* **11**, 274–284 (2017).
12. Arbabi, A. & Faraon, A. Advances in optical metalenses. *Nat. Photonics* **17**, 16–25 (2023).
13. Li, Z. et al. Optical polarization manipulations with anisotropic nanostructures. *Photonix* **5**, 30 (2024).
14. Dai, C., Liu, T., Wang, D. & Zhou, L. Multiplexing near- and far-field functionalities with high-efficiency bi-channel metasurfaces. *Photonix* **5**, 11 (2024).
15. Joannopoulos, J. D., Villeneuve, P. R. & Fan, S. Photonic crystals: putting a new twist on light. *Nature* **386**, 143–149 (1997).
16. Joannopoulos, J. D., Johnson, S. G., Winn, J. N. & Meade, R. D. *Photonic Crystals Molding the Flow of Light - Second Edition*. REV - Revised, 2 edn, (Princeton University Press, 2008).
17. Hafezi, M., Demler, E. A., Lukin, M. D. & Taylor, J. M. Robust optical delay lines with topological protection. *Nat. Phys.* **7**, 907–912 (2011).
18. Ma, T. & Shvets, G. All-Si valley-Hall photonic topological insulator. *N. J. Phys.* **18**, 025012 (2016).
19. Rechtsman, M. C. et al. Photonic Floquet topological insulators. *Nature* **496**, 196–200 (2013).
20. Harari, G. et al. Topological insulator laser: theory. *Science* **359**, eaar4003 (2018).
21. Bandres, M. A. et al. Topological insulator laser: experiments. *Science* **359**, eaar4005 (2018).
22. Zeng, Y. et al. Electrically pumped topological laser with valley edge modes. *Nature* **578**, 246–250 (2020).
23. Khanikaev, A. B. & Shvets, G. Two-dimensional topological photonics. *Nat. Photonics* **11**, 763–773 (2017).
24. Wu, L.-H. & Hu, X. Scheme for achieving a topological photonic crystal by using dielectric material. *Phys. Rev. Lett.* **114**, 223901 (2015).
25. Mittal, S., Orre, V. V., Leykam, D., Chong, Y. D. & Hafezi, M. Photonic anomalous quantum hall effect. *Phys. Rev. Lett.* **123**, 043201 (2019).
26. Liang, G. Q. & Chong, Y. D. Optical resonator analog of a two-dimensional topological insulator. *Phys. Rev. Lett.* **110**, 203904 (2013).
27. Yang, H. et al. Optically Reconfigurable spin-valley hall effect of light in coupled nonlinear ring resonator lattice. *Phys. Rev. Lett.* **127**, 043904 (2021).
28. Gladstone, R. G., Jung, M., Han, Y. & Shvets, G. Photonic emulation of two-dimensional materials with antiferromagnetic order. *Phys. Rev. B* **100**, 245417 (2019).
29. Hafezi, M., Mittal, S., Fan, J., Migdall, A. & Taylor, J. M. Imaging topological edge states in silicon photonics. *Nat. Photonics* **7**, 1001–1005 (2013).
30. Khanikaev, A. B. et al. Photonic topological insulators. *Nat. Mater.* **12**, 233–239 (2013).
31. Ma, T., Khanikaev, A. B., Mousavi, S. H. & Shvets, G. Guiding electromagnetic waves around sharp corners: topologically protected photonic transport in metawaveguides. *Phys. Rev. Lett.* **114**, 127401 (2015).
32. Yin, X., Ye, Z., Rho, J., Wang, Y. & Zhang, X. Photonic spin Hall effect at metasurfaces. *Science* **339**, 1405–1407 (2013).
33. Kapitanova, P. V. et al. Photonic spin Hall effect in hyperbolic metamaterials for polarization-controlled routing of subwavelength modes. *Nat. Commun.* **5**, 3226 (2014).
34. Sala, V. G. et al. Spin-orbit coupling for photons and polaritons in microstructures. *Phys. Rev. X* **5**, 011034 (2015).
35. Mermin, N. D. The topological theory of defects in ordered media. *Rev. Mod. Phys.* **51**, 591–648 (1979).
36. Li, X., Cao, T., Niu, Q., Shi, J. & Feng, J. Coupling the valley degree of freedom to antiferromagnetic order. *Proc. Natl. Acad. Sci. USA* **110**, 3738–3742 (2013).
37. Liu, T., Yan, W. & Qiu, M. Bending immunity in valley edge states and non-Hermitian supercoupling effects. *Phys. Rev. B* **110**, L020101 (2024).
38. Colomés, E. & Franz, M. Antichiral edge states in a modified haldane nanoribbon. *Phys. Rev. Lett.* **120**, 086603 (2018).
39. Zhou, P. et al. Observation of photonic antichiral edge states. *Phys. Rev. Lett.* **125**, 263603 (2020).
40. Xie, L., Jin, L. & Song, Z. Antihelical edge states in two-dimensional photonic topological metals. *Sci. Bull.* **68**, 255–258 (2023).
41. Zhao, Y. X., Chen, C., Sheng, X.-L. & Yang, S. A. Switching spinless and spinful topological phases with projective  $\mathbb{Z}_2$  Symmetry. *Phys. Rev. Lett.* **126**, 196402 (2021).
42. Zhao, Y. X., Huang, Y.-X. & Yang, S. A.  $\mathbb{Z}_2$ -projective translational symmetry protected topological phases. *Phys. Rev. B* **102**, 161117 (2020).
43. Xue, H. et al. Projectively enriched symmetry and topology in acoustic crystals. *Phys. Rev. Lett.* **128**, 116802 (2022).
44. Li, T. et al. Acoustic  $\mathbb{Z}_2$  insulators from projective symmetry. *Phys. Rev. Lett.* **128**, 116803 (2022).

## Acknowledgements

We thank Thomas Christensen, Wenbu Duan for fruitful discussions and suggestions.

## Author contributions

All authors made substantial contributions to this work. W. Y. initiated and supervised this project with M. Q., and T. L. performed the daily project supervision.

## Competing interests

The authors declare no competing interests.

## Additional information

**Supplementary information** The online version contains supplementary material available at <https://doi.org/10.1038/s41467-025-67627-2>.

**Correspondence** and requests for materials should be addressed to Min Qiu or Wei Yan.

**Peer review information** *Nature Communications* thanks Alexander Khanikaev and the other, anonymous, reviewer(s) for their contribution to the peer review of this work. A peer review file is available.

**Reprints and permissions information** is available at <http://www.nature.com/reprints>

**Publisher's note** Springer Nature remains neutral with regard to jurisdictional claims in published maps and institutional affiliations.

**Open Access** This article is licensed under a Creative Commons Attribution-NonCommercial-NoDerivatives 4.0 International License, which permits any non-commercial use, sharing, distribution and reproduction in any medium or format, as long as you give appropriate credit to the original author(s) and the source, provide a link to the Creative Commons licence, and indicate if you modified the licensed material. You do not have permission under this licence to share adapted material derived from this article or parts of it. The images or other third party material in this article are included in the article's Creative Commons licence, unless indicated otherwise in a credit line to the material. If material is not included in the article's Creative Commons licence and your intended use is not permitted by statutory regulation or exceeds the permitted use, you will need to obtain permission directly from the copyright holder. To view a copy of this licence, visit <http://creativecommons.org/licenses/by-nc-nd/4.0/>.

© The Author(s) 2025